

See discussions, stats, and author profiles for this publication at: <https://www.researchgate.net/publication/231647784>

# 3D Imaging of Catalyst Support Corrosion in Polymer Electrolyte Fuel Cells

ARTICLE in THE JOURNAL OF PHYSICAL CHEMISTRY C · JULY 2011

Impact Factor: 4.77 · DOI: 10.1021/jp203016u

CITATIONS

57

READS

744

8 AUTHORS, INCLUDING:



[Hendrik Schulenburg](#)

Metrohm AG

21 PUBLICATIONS 697 CITATIONS

SEE PROFILE



[Roman Grothausmann](#)

26 PUBLICATIONS 170 CITATIONS

SEE PROFILE




[Ingo Manke](#)

Helmholtz-Zentrum Berlin

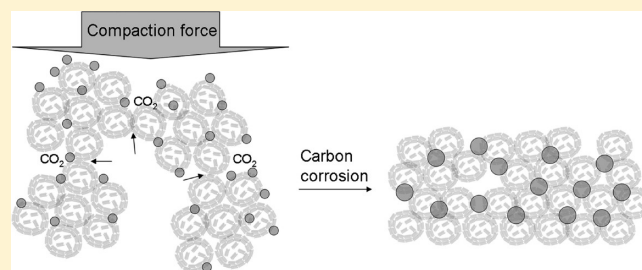
294 PUBLICATIONS 4,448 CITATIONS

SEE PROFILE

# 3D Imaging of Catalyst Support Corrosion in Polymer Electrolyte Fuel Cells

Hendrik Schulenburg,<sup>\*,†</sup> Bernhard Schwanitz,<sup>†</sup> Nicolas Linse,<sup>†</sup> Günther G. Scherer,<sup>†</sup> and A. Wokaun<sup>†</sup><sup>†</sup>General Energy Research Department, Paul Scherrer Institut, CH-5232 Villigen, SwitzerlandJulijana Krbanjevic<sup>‡</sup><sup>‡</sup>Centre de Recherches en Physique des Plasmas, École Polytechnique Fédérale de Lausanne, Association Euratom-Confédération Suisse, CH-5232 Villigen PSI, SwitzerlandRoman Grothausmann<sup>§</sup> and Ingo Manke<sup>§</sup><sup>§</sup>Institute Applied Materials, Helmholtz Zentrum für Materialien und Energie, Hahn-Meitner-Platz 1, D-14109 Berlin, Germany Supporting Information Web-Enhanced

**ABSTRACT:** During the lifetime of a polymer electrolyte fuel cell, the pore structure of the Pt/C catalyst layer may change as a result of carbon corrosion. Three-dimensional visualization of porosity changes is important to understand the origin of fuel cell performance deterioration. A focused ion beam/scanning electron microscopy (FIB/SEM) approach was adopted together with electron tomographic studies to visualize the three-dimensional pore structure of a Pt/C catalyst. In the case of pristine catalyst layers, the pores form an interconnected network. After 1000 start-up/shut-down cycles, severe carbon corrosion leads to a collapse of the support structure. The porosity of the degraded catalyst layer shrinks drastically, resulting in a structure of predominantly isolated pores. These porosity changes hinder the mass transport in the catalyst layer, consequently leading to a substantial loss of fuel cell performance. FIB/SEM serial sectioning and electron tomography allows three-dimensional imaging of the catalyst pore structure, which is a prerequisite for modeling and optimizing mass transport in catalyst layers.



## 1. INTRODUCTION

In heterogeneous catalyst systems, the pore structure of the support is paramount to the transport of educts and products.<sup>1</sup> Structure and dimensional stability of the support have a great impact on the rate of the catalyzed reaction. Quantification and visualization of porosity changes during the lifetime of a supported catalyst is crucial for a systematic development of durable catalyst layers. By using gas adsorption methods or mercury porosimetry, pore size distributions are accessible; however, these methods do not yield information about the pore structure and connectivity. To obtain a comprehensive view of catalyst support degradation, a visualization of porosity changes at the nanoscale is desirable.

In polymer electrolyte fuel cells (PEFCs), carbon-supported Pt or Pt-alloy nanoparticles are the catalyst of choice. They catalyze both the anodic hydrogen oxidation and the cathodic oxygen reduction reaction. Especially under dynamic operating conditions, PEFC performance can deteriorate rapidly, which is one of the reasons why PEFC technology has not been introduced into the mass market, for example, for automotive applications.<sup>2,3</sup> Generally, two main degradation processes can

be distinguished with respect to catalyst deterioration. First, sintering, dissolution, and redeposition of platinum can reduce the electrochemically active Pt surface area (ECA). Second, corrosion of the carbon support<sup>4–18</sup> (cf. eq 1) may lead to particle detachment<sup>18,19</sup> and changes of the catalyst layer porosity.<sup>4,5</sup>



The pore structure of the cathode catalyst layer is critical to transport of oxygen to active sites and removal of product water. Therefore, carbon-corrosion-induced porosity changes can significantly contribute to fuel cell performance loss. Both processes, loss of active Pt surface area and carbon support corrosion, are strongly promoted by elevated potentials (>1 V) and fast potential transients.<sup>2–4,6–10,12,14,17,19–22</sup>

In this work, we employed focused ion beam/scanning electron microscopy (FIB/SEM) serial sectioning to visualize

Received: March 31, 2011

Revised: May 30, 2011

Published: June 07, 2011

porosity changes in catalyst layers of PEFCs. This method has been used to image 3D structures of solid oxide fuel cell electrodes<sup>23–26</sup> or pristine PEFC catalysts.<sup>27–30</sup> We applied this method to study morphological changes of the catalyst layers before and after PEFC durability tests. Catalyst-coated membranes (CCMs) were subjected to two different degradation protocols. Start-up and shut-down conditions of a PEFC were simulated by alternating purging of the anode compartment with hydrogen and air. In a second degradation experiment, a cell was cycled between 0.6 V and the open-circuit voltage (OCV). The three-dimensional pore structure before and after electrochemical degradation was investigated by FIB/SEM serial sectioning. In addition, the FIB/SEM was used to prepare transmission electron microscopy (TEM) lamellae to study changes in the catalyst support morphology by electron tomography.

We will show that both degradation protocols lead to a comparable increase of the Pt particle size in the cathode catalyst layer. After potential cycling, neither catalyst support porosity nor fuel cell performance changed markedly. The severe loss of performance observed after start/stop cycling was ascribed to a collapse of the pore structure including the formation of isolated pores.

## 2. EXPERIMENTAL METHODS

**2.1. Electrochemical degradation.** For PEFC degradation experiments, catalyst-coated membranes (CCMs), supplied by W.L. Gore & Associates (PRIMEA MEA Series 5710), with a cathode loading of 0.4 mg<sub>Pt</sub>/cm<sup>2</sup> and an anode loading of 0.1 mg<sub>Pt</sub>/cm<sup>2</sup> were used. The specified membrane thickness was 18 μm. Gas diffusion layers with a microporous layer (BASF, E-TEK division, type LT1410W) were used on the anode and cathode side. All electrochemical degradation experiments were carried out in a 16 cm<sup>2</sup> single cell with parallel flow fields.

For start/stop cycling, the fuel cell anode was alternately purged with H<sub>2</sub> and air (60s/60s), while air was continuously fed to the cathode compartment. During the experiment, an external load of 3 mΩ cm<sup>2</sup> was applied. At 80 °C and 70% relative humidity (RH), 1000 start/stop cycles were accumulated (Figure 1a). In a second degradation experiment, the cathode was exposed to a square wave potential between 0.6 V and the open-circuit potential. The potential was cycled a total of 24 000 times, at a time step of 10 s for each potential (Figure 1b). The cell was operated at 80 °C using fully humidified H<sub>2</sub> and O<sub>2</sub> at a stoichiometry of 1.5/1.5. The CO<sub>2</sub> concentration in the cathode exhaust was monitored using a model 100 infrared analyzer (California Analytical Instruments, U.S.A.) (Figure 1c,d).

**2.2. Focused Ion Beam Scanning Electron Microscopy (FIB/SEM) Serial Sectioning.** For FIB/SEM serial sectioning, a Zeiss NVision 40 microscope was employed. In preparation for FIB/SEM measurements, the gas diffusion layers of the degraded CCMs were gently removed with two tweezers. Afterward, the samples were glued using conductive carbon dispersion (Leit-C after Göcke, Neubauer Chemikalien, Germany) to an aluminum sample holder with the cathode layer on top. Columnar structures of the catalyst layers were prepared by ion milling. These were covered with a smooth carbon layer to minimize curtain effects.<sup>31</sup> Serial sectioning was performed using a focused Ga<sup>+</sup> beam at an acceleration voltage of 30 kV and one section every ~10 nm in the z-direction. The slice thickness was calculated by dividing the total eroded thickness in the z-direction by the number of sections. The automated imaging of each section by

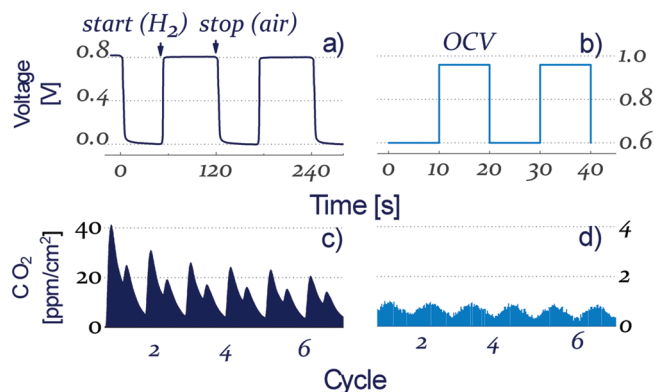


**Figure 1.** (a) PEFC catalyst degradation protocols for start/stop cycling, with the anode alternately purged with H<sub>2</sub> and air (60s/60s), the cathode purged with air, an external load of 3 mΩ cm<sup>2</sup>, 80 °C, 70% relative humidity (RH), and 1000 cycles. (b) Degradation protocol for potential cycling between 0.6 V and the open circuit voltage, with a time step of 10 s, H<sub>2</sub>/O<sub>2</sub> at ambient pressure and 1.5/1.5 stoichiometry, 100% RH, 80 °C, and 24 000 cycles. (c) CO<sub>2</sub> concentration measured in the cathode exhaust during start/stop cycling and (d) potential cycling.

SEM was done at a magnification of 300 000× at an acceleration voltage of 3 kV. A secondary electron in the lens detector was used. Reconstruction of the three-dimensional image and calculation of the porosity were performed using Avizo-Standard 5.1 software (VSG, U.S.A.). For each sample, two cuboids from different locations of the catalyst layer were analyzed.

Calculation of 3D images out of the single micrographs requires proper alignment and segmentation. Thereby, discrimination between pores and bulk material is a crucial step in image processing. In recent FIB/SEM studies of Ender<sup>32</sup> and Wilson,<sup>26</sup> the cathode of a lithium ion battery was embedded in a silicon or epoxy resin to facilitate the discrimination of pore volume and material. Filling the pore volume of the fuel cell catalysts with a resin or liquid metal<sup>28,33</sup> did not facilitate the discrimination of pores and material in our study. The reason for this is probably the composition and morphology of the Pt/C catalysts. The Pt particles are too small to be resolved (diameter ≈ 2–5 nm) by SEM and are not always homogeneously dispersed on the carbon support. Therefore, the Z-contrast of the material (Pt/C) can vary significantly. Areas with high and low Pt loadings and thereby high and low Z-contrast are present, in particular after degradation. If the Pt/C catalysts are embedded in an epoxy resin, it can be difficult to distinguish between resin and catalyst areas with low Pt loading. Also, embedding the catalyst in Woods metal did not allow the discrimination of pore and material. The difference in the Z-contrast of the catalyst and Woods metal is too low.

Therefore, we choose an approach for segmentation of SEM images without prior embedding of the sample.<sup>27–30</sup> Because the SEM images have a finite depth of focus, the pore/material discrimination can be ambiguous if single SEM images are inspected. Several processing steps are necessary to obtain reliable results. First, we optimized SEM parameters including detector type and acceleration voltage to obtain the highest possible resolution with a minimum depth of focus. Second, we assigned appropriate ranges of bright gray to the “material” and darker gray to the “pores” by visual inspection. This assignment, however, is not unambiguous in all cases. Regions possessing similar gray scale values may be located at different positions in

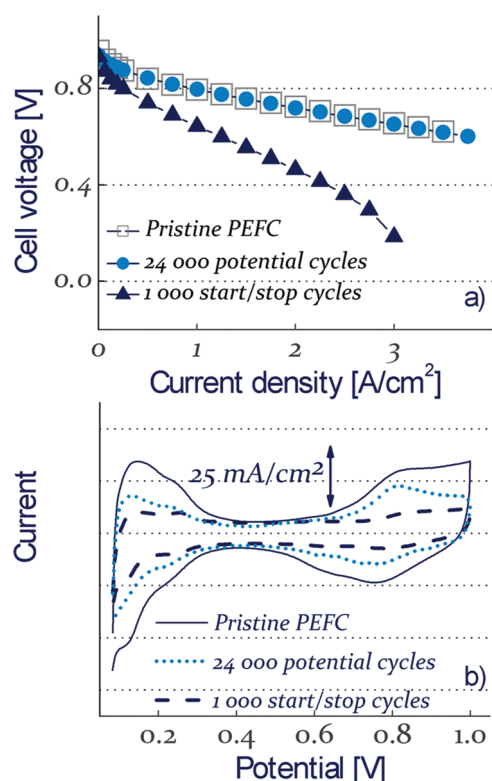


**Figure 2.** (a) Fuel cell performance at 80 °C, 100% RH, and  $\text{H}_2/\text{O}_2 = 1.5/1.5$  at 2.5 bar<sub>abs</sub>; (b) cyclic voltammograms measured in  $\text{H}_2/\text{N}_2$  mode, at 80 °C, 100 mV/s, and 2.5 bar<sub>abs</sub>.

the  $z$ -direction, where  $z$  represents the depth of the volume of interest.

To correct for this effect, successive images were analyzed to determine if the shape of the material region changes or not. If changes were observed, the respective region was assumed to be located at the machined surface and is therefore assigned as material. If the shape of the inspected material does not change in successive images, the material is obviously not in but below the machined surface. Therefore, those regions were assigned as pores. The whole set of images is segmented in this way.

Prior to calculation of the pore size distribution, the resolution in the  $x$ - and  $y$ -directions was reduced to obtain cubic voxels. The pore size distribution was calculated from the 3D images by using the local thickness function in Fiji open source software.<sup>49</sup> Hereby, a volume-based local thickness is estimated by fitting spheres of maximal diameter into the pore structure.<sup>34</sup>

**2.3. TEM Lamellae Preparation.** The Zeiss NVision 40 microscope was also employed to mill TEM lamellae of the pristine and degraded cathode catalyst layers. The carbon frames ( $\sim 1 \mu\text{m}$  thickness) were obtained by site-specific decomposition of phenanthrene gas by secondary electrons generated by the incident focused  $\text{Ga}^+$  ion beam (30 kV). In the same manner, the lamellae were attached to copper lift-out grids (J422, Plano GmbH, Germany). A Phillips CM30 microscope (300 kV) was used for TEM determination of the Pt particle size. Mean particle sizes were determined using the UTHSCSA Image tool 3.0 (UT Health Science Center, San Antonio, U.S.A.) by measuring several hundred particles in different regions of the lamellae. Unless otherwise noted, the FIB/SEM was operated at room temperature.

**Table 1.** Degradation Parameter of PEFC Cathode Catalyst Layers

	pristine	potential cycling <sup>a</sup>	start/stop cycling <sup>a</sup>
cell voltage at 1 A/cm <sup>2</sup> [mV]	794	796	643
$H_{\text{upd}}$ surface area [m <sup>2</sup> /g <sub>Pt</sub> ]	57	14	9
mean Pt particle size <sup>b</sup> [nm]	2.3	4.8	5.3
CO <sub>2</sub> evolution [μg C/cycle]		0.04	1.85
overall porosity <sup>c</sup> [%]	40 ± 3	36 ± 3	5 ± 3
closed porosity <sup>c</sup> [%]	0	0	2 ± 2

<sup>a</sup> Degradation protocol; compare Figure 1. <sup>b</sup> Determined by TEM.

<sup>c</sup> Determined by FIB/SEM.

**2.4. Electron Tomography.** Electron tomography experiments on TEM lamellae were performed with a Zeiss LIBRA 200FE transmission electron microscope (TEM) at the Helmholtz Centre Berlin for Materials and Energy (HZB). The method and its application to heterogeneous catalyst materials were described earlier by Frank,<sup>33</sup> Grothausmann,<sup>36</sup> and Friedrich.<sup>37</sup> The energy filter was used to record zero-loss (ZL) images at 200 keV while the sample was tilted from around  $-70$  to  $70^\circ$  with an angular increment of  $0.5^\circ$ . The  $x$ - $y$ - $z$ -tracking<sup>38</sup> was done by the digital micrograph tomography module (Gatan). The images were aligned by tracking platinum particles within the sample with IMOD.<sup>39</sup> The tomographic reconstruction was performed by WBP (weighted back projection, IMOD).

### 3. RESULTS AND DISCUSSION

**3.1. Electrochemical Characterization.** Polarization curves measured in  $\text{H}_2/\text{O}_2$  mode before and after the degradation experiments are displayed in Figure 2a. After 24 000 potential cycles, PEFC performance is almost unchanged. In contrast, a distinct performance loss especially at higher current densities was observed after 1000 start/stop cycles. Degradation of the membrane is negligible in both cases (Figure S1, Supporting Information).

Despite the strongly differing performance loss rates, both degradation experiments lead to comparable Pt particle growth and loss of electrochemically active surface area (ECA) (Figure 2b and Table 1). The ECA loss is therefore unlikely to be solely responsible for performance deterioration in the case of start/stop cycling. The pronounced performance loss at high current densities indicates increased mass-transport losses.

Corrosion of the carbon support material can be quantified by measuring the CO<sub>2</sub> concentration in the cathode exhaust gas (cf. eq 1). In the case of potential cycling, the potential at the positive electrode never exceeds the open-circuit voltage of about 960 mV. Therefore, CO<sub>2</sub> evolution is very low (Figure 1d, Table 1). During start/stop cycling, however, the positive electrode is exposed to potentials significantly higher than 1 V.<sup>40</sup> These elevated potentials lead to a strong intensification of carbon corrosion, thus resulting in a distinct CO<sub>2</sub> peak during fuel cell start-up and shut-down, respectively (Figure 1c).

**3.2. FIB/SEM Serial Sectioning.** Representative SEM images of the catalyst layers before and after start/stop degradation are shown in Figure 3. The low magnification image (Figure 3a) shows the dissected columnar volume of interest of a pristine catalyst layer, while Figure 3b displays a high magnification SEM image of the same material. In these images, pores appear dark



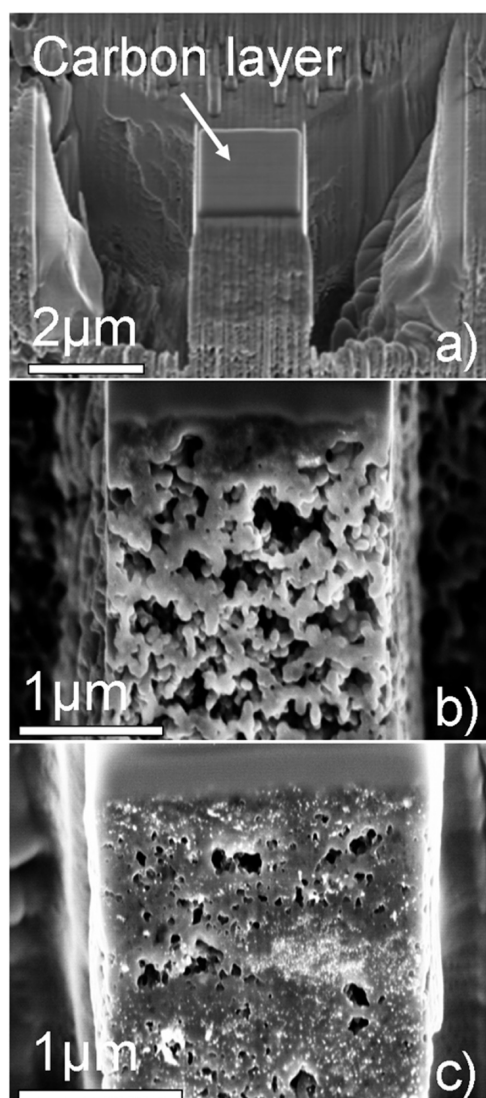


**Figure 3.** (a) The PEFC cathode catalyst layer before degradation; dissected columnar volume of interest. (b) SEM image taken during FIB/SEM serial sectioning of the pristine cathode catalyst layer. (c) SEM image after start/stop degradation.

gray. The large porosity of the pristine catalyst layer is obvious. After start/stop cycling (Figure 3c), the fraction of dark gray pixels shrinks drastically. A substantial decrease in porosity is observed. In contrast to start/stop cycling, SEM images after potential cycling are very similar to images of the pristine catalyst layer.

The three-dimensional pore structure of the cathode catalyst layer before and after start/stop cycling is shown in Figure 4. A typical voxel size in these images is  $2.5 \times 2.5 \times 10$  nm in the  $x$ -,  $y$ -, and  $z$ -directions. This voxel size allows for imaging of the majority of the pore volume, although micropores such as those in carbon black primary particles or small mesopores cannot be resolved.<sup>5</sup> In this context, our definition of micro- and mesopore size follows the recommendations of the International Union of Pure and Applied Chemistry (IUPAC), that is, micropores have diameters smaller than 2 nm, while mesopores have diameters between 2 and 50 nm.

The calculated pore structures of the pristine and the potential cycled catalyst layers do not exhibit significant differences. In

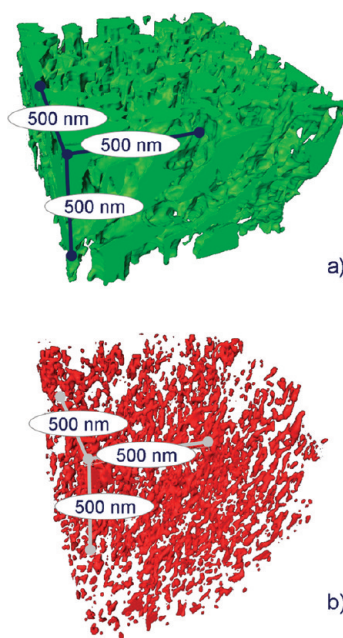


**Figure 4.** Three-dimensional pore structure of the pristine cathode catalyst layer (a) and after start/stop cycling (b). The colored phase represents the pore structure. Movies in mpg format of the pristine and degraded cathode pore structure are provided.

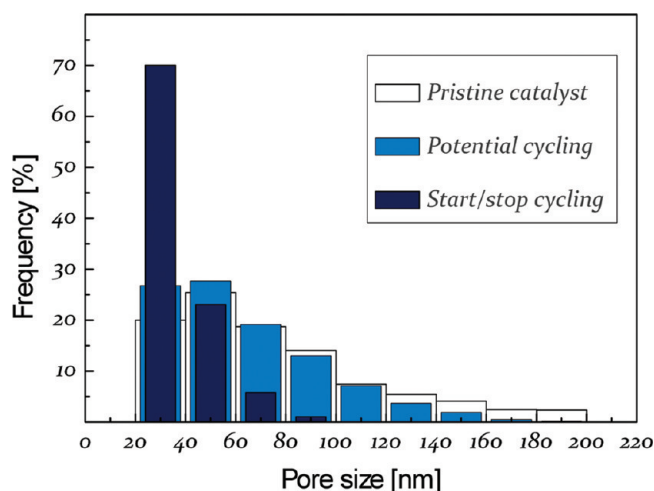


**Figure 5.** Pore size distribution of the cathode catalyst layer determined by FIB/SEM serial sectioning, 20 nm increments.

both cases, the pores form an interconnected network with a porosity of around 40% (Table 1). In contrast, start/stop cycling causes a significant change in the catalyst layer morphology. As a result of severe carbon corrosion, the calculated porosity drops to 5%. Moreover, the average pore size decreases, and the previously interconnected pore network changes to a structure of predominantly isolated pores. In the pristine catalysts and after potential cycling, no isolated pores can be detected, whereas a large fraction of the pore volume is not interconnected after start/stop cycling. Figure 5 displays the pore size distributions calculated from the corresponding 3D images. The resolution is limited by the slice thickness of  $\sim 10$  nm. For this reason, pores with a diameter  $< 20$  nm cannot be resolved. The pore size

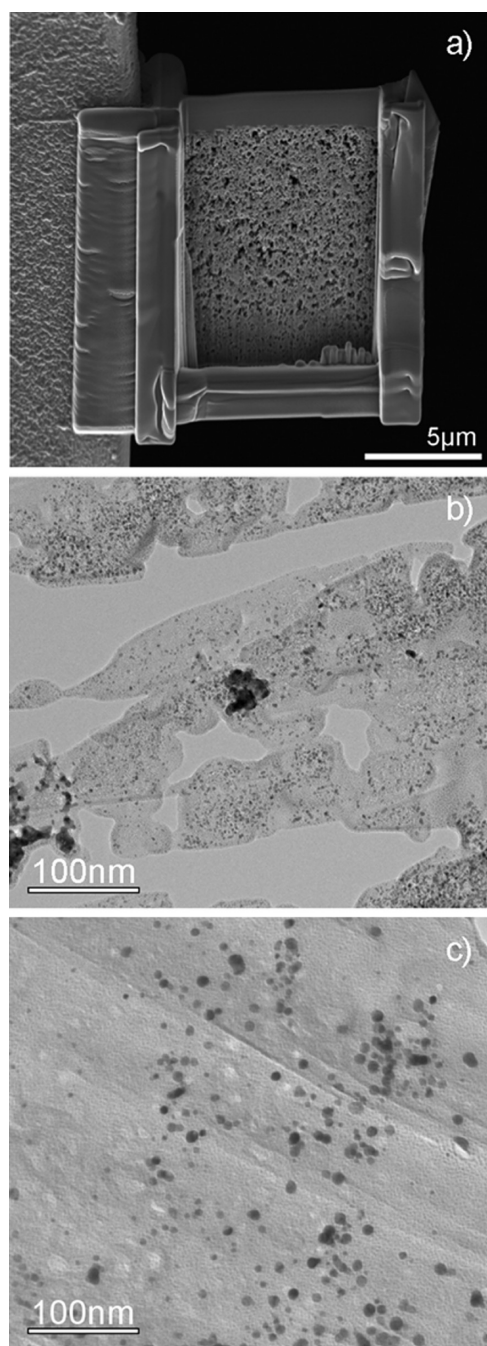


**Figure 6.** (a) TEM lamella of the pristine cathode catalyst layer attached to a lift-out grid. The carbon frame was prepared by site-specific chemical vapor deposition of phenanthrene; (b) pristine catalyst layer; (c) after start/stop degradation.

distribution before and after potential cycling is very similar. Roughly, 50% of the detectable pores are smaller than 60 nm. The diameter of the pores in the fresh catalyst layer and after potential cycling can be as high as 200 nm. After start/stop degradation, the fraction of macropores shrinks significantly. Most of the remaining detectable pores are mesopores.

FIB milling causes heating of the machined surface and may damage the investigated material. Amorphization of materials with poor heat conductivity, for example, silicon or other semiconductors, has been reported.<sup>41,42</sup> This heating could also

influence the determination of the fuel cell catalyst porosity and 3D structure. To avoid an influence of the FIB on the 3D structure of the catalysts, a low-voltage FIB was used (30 kV). To assess the influence of heating, we additionally carried out cryo-FIB/SEM serial sectioning of the pristine catalyst layer at  $\sim 77$  K. The calculated porosity was virtually the same as compared to that of room-temperature FIB/SEM serial sectioning. The high electron and heat conductivity of the catalyst layers obviously prevents significant damage of the porous catalyst structure.

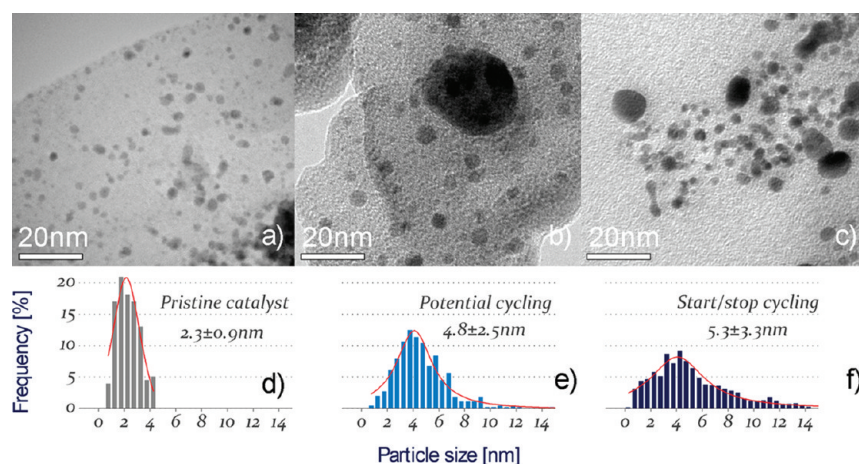
**3.3. TEM Lamellae Investigation.** The FIB/SEM was also used to prepare TEM lamellae for analysis of the Pt particle size and the carbon support structure. TEM lamellae of the catalyst layers do not require prior embedding in an epoxy resin. Therefore, the TEM images provide information not only about the Pt particle size but also about the carbon morphology.

Figure 6 shows a TEM lamella of the pristine catalyst layer at low (Figure 6a) and high magnification (Figure 6b), while a high-magnification image after start/stop cycling can be seen in Figure 6c. TEM images of the pristine catalyst layer (Figure 6b) show the expected highly porous carbon support structure, which is also observed after potential cycling. After start/stop cycling (Figure 6c), the carbon support looks like a dense film. Platinum particles seem to be embedded in a carbon matrix. Bright round shapes with a typical diameter of  $<50$  nm may be assigned to pores that were also detected in the corresponding 3D image (Figure 4b). Figure 7 illustrates the changes of the Pt particle size before and after degradation. TEM images of the pristine (Figure 7a) and degraded cathode catalyst layers (Figure 7b and c) show that both degradation protocols lead to a comparable Pt particle growth (Figure 7d–f). The mean particle size increases from 2.3 nm in the pristine catalyst to 4.8 nm after potential cycling and 5.3 nm after start/stop cycling.

Even after start/stop cycling and the collapse of the carbon support structure, the fuel cell performance is reasonable. At a current density of  $1 \text{ A/cm}^2$ , the cell voltage drops from 794 to 643 mV. This is surprising because FIB/SEM indicates that a large part of the pores are isolated and the carbon structure of the TEM lamellae looks like a dense film. According to the images, it seems to be very difficult for oxygen molecules and protons to reach active Pt sites; therefore, more pronounced fuel cell performance loss would have been expected. The just moderate fuel cell performance loss after start/stop cycling may be explained by the presence of small interconnected pores that cannot be resolved by FIB/SEM. To verify this hypothesis, a 3D imaging method with higher resolution is required, that is, electron tomography.

**3.4. Electron Tomography.** Electron tomography was carried out using TEM lamellae of the pristine and start/stop cycled cathode catalyst layer. After image acquisition, alignment, and reconstruction, the resulting 3D images can be investigated. Sliced cross-sectional images or “digital slices”<sup>43</sup> of the pristine cathode are shown in Figure 8. The low-magnification image shows a cross section of an agglomerate of several carbon black primary particles. It is noteworthy that even before degradation, Pt particles were found also inside of the primary particles. In a recent 3D TEM study by Ito,<sup>43</sup> the Pt particles of a Pt/Vulcan catalyst were found to be located only at the external surface of primary particles, although the Pt particles were more or less embedded in the surface. The carbon primary particles used in our study are obviously more porous, thus allowing the infiltration of Pt particles during the catalyst synthesis. A similar distribution of metal nanoparticles in high-surface-area carbon





**Figure 7.** TEM images of (a) the pristine cathode catalyst layer, (b) after potential cycling, and (c) after start/stop degradation. (d–f) Corresponding Pt particle size distributions.

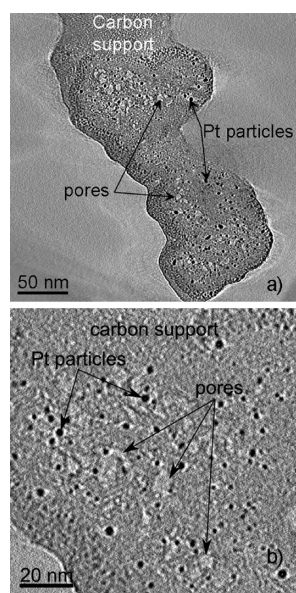


**Figure 8.** Electron tomogram slices of the pristine cathode catalyst layer at (a) low resolution and (b) high resolution.

was observed in a 3D TEM study of Ru/black pearls.<sup>44</sup> Numerous bright roundish sites detected within the carbon particles might be assigned as mesopores (Figure 8a,b).

After start/stop induced degradation (Figure 9), the collapsed carbon support structure still exhibits mesopores that are also observed in the FIB/SEM analysis (Figure 4b). These mesopores are a frequent feature after start/stop degradation. TEM images taken from the tilt series of the degraded sample confirm that pores with diameters between 5 and 20 nm exist, which are too small to be resolved by FIB/SEM. These pores appear light gray in Figure 10 and the associated video clip. These small mesopores are usually isolated. This morphological change of the carbon support leads to Pt particles mostly embedded inside of the carbon structure with no or limited connection to the gas supply. Very few macropores are still present and might connect the embedded Pt particles with the surface.

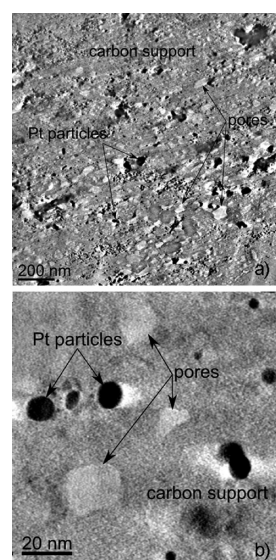


**Figure 9.** Electron tomogram slices of the start/stop degraded cathode catalyst layer at (a) low resolution and (b) high resolution.

The rendered images in Figure 11 and the corresponding video clips visualize the difference in carbon support morphology before and after start/stop induced degradation. In these images, Pt particles are shown in green, the carbon support is gray, and the pores in the carbon support are light gray. Figure 11a illustrates the expected carbon black structure of the pristine catalyst, consisting of connected carbon primary particles. After start/stop degradation (Figure 11b), the carbon support structure is very dense. The meander-like structure of the TEM lamella after degradation (Figure 11b) is due to the curtain effect during ion milling by the FIB.

**3.5. Catalyst Layer Morphology after Start/Stop Cycling.** Start/stop induced degradation leads to a cathode catalyst layer morphology that hinders the transport of oxygen to active sites and removal of product water. The carbon support pore structure changes from an interconnected network to a dense carbon layer with mainly isolated pores. Although start/stop induced porosity changes are drastic in

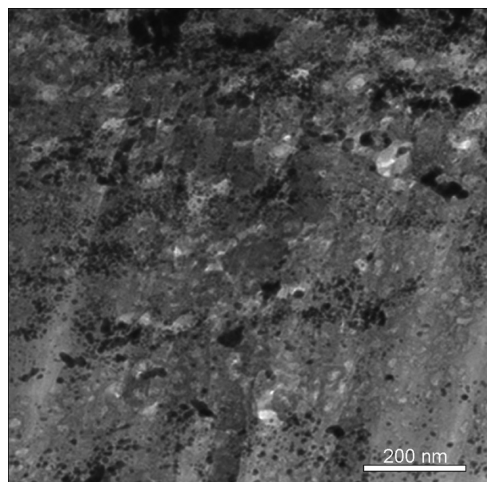


**Figure 10.** ZL-TEM image of the start/stop cycled cathode catalyst layer. A movie in avi format of the tilt series is provided.

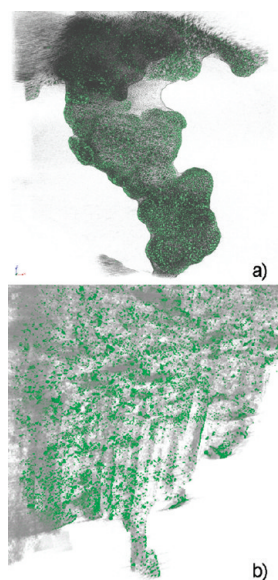


**Figure 11.** Volume rendered images of (a) the pristine cathode catalyst layer and that (b) after start/stop degradation. Movies in avi format of the pristine and degraded cathode catalyst layer are available.

our study, carbon loss, which was calculated from the total amount of  $\text{CO}_2$  generated over the course of the experiment, is relatively low ( $\sim 8\%$ ). This finding suggests a collapse of the porous structure caused by corrosion-induced weakening of the connections between single carbon primary particles. Such a “neck-breaking” was discussed by Liu,<sup>4</sup> who investigated Pt/Vulcan catalysts by identical location TEM. Moreover, carbon corrosion studies<sup>45–48</sup> show that Pt catalyzes the carbon corrosion during start/stop degradation experiments. Therefore, the neck-breaking might be catalyzed by Pt particles located at the interface of connected carbon particles. Because the assembly of the fuel cell leads to a compaction force on the CCM, these loosely or nonconnected primary particles may form the observed relatively dense carbon structure with mainly isolated pores and embedded Pt particles (Figure 12).

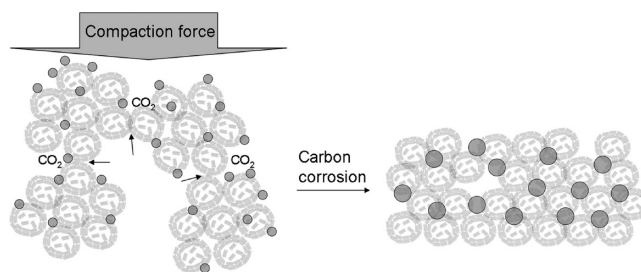


**Figure 12.** Proposed mechanism for the structural changes of the cathode catalyst layer during start/stop degradation. Carbon corrosion at the surface of primary particles leads to neck-breaking (arrows). This process may be catalyzed by Pt particles. The compaction force in the membrane electrode assembly leads to the formation of a low-porosity carbon structure with a large fraction of embedded Pt particles.

#### 4. CONCLUSIONS

A PEFC catalyst-coated membrane was subject to two degradation protocols. Degradation by potential cycling (24000 cycles, 0.6 V-OCV) and start/stop cycling (1000 cycles) leads to a comparable loss of the active Pt surface area in the cathode catalyst layers. Despite this surface area loss, the potential cycled cathode still provides enough accessible active sites to maintain the initial fuel cell performance. In contrast to potential cycling, start/stop cycling causes significant corrosion of the carbon support at the fuel cell cathode. The resulting decrease in porosity and pore size of the carbon support hinders mass transport, leading to severe fuel cell performance loss. FIB/SEM serial sectioning and electron tomography allow the quantification and visualization of these porosity changes. The calculated pore structures, porosity values, and pore size distributions are a prerequisite to understanding and modeling mass transport in catalyst layers.

#### ■ ASSOCIATED CONTENT

**Supporting Information.** Hydrogen permeation current measurements and Nyquist plots before and after degradation. This material is available free of charge via the Internet at <http://pubs.acs.org>.

**Web Enhanced Feature.** Movies of the pristine and degraded cathode pore structure, of the tilt series, and of the pristine and degraded cathode catalyst layer are available in the HTML version of the paper.

#### ■ AUTHOR INFORMATION

##### Corresponding Author

\*Fax: +041 56 310 4415. E-mail: [hendrik.schulenburg@psi.ch](mailto:hendrik.schulenburg@psi.ch).

#### ■ ACKNOWLEDGMENT

The authors acknowledge L. Gubler and R. Schäublin (PSI) for helpful discussion. Dedicated to Professor Manfred T. Reetz on the occasion of his retirement as director of the Max-Planck-Institut für Kohlenforschung.

#### ■ REFERENCES

- (1) Hagen, J. *Industrial Catalysis: A Practical Approach*, 2nd ed.; Wiley-VCH Verlag: Weinheim, Germany, 2006.



- (2) de Bruijn, F. A.; Dam, V. A. T.; Janssen, G. J. M. *Fuel Cells* **2008**, *8*, 3.
- (3) Borup, R.; Meyers, J.; Pivovar, B.; Kim, Y. S.; Mukundan, R.; Garland, N.; Myers, D.; Wilson, M.; Garzon, F.; Wood, D.; Zelenay, P.; More, K.; Stroh, K.; Zawodzinski, T.; Boncella, J.; McGrath, J. E.; Inaba, M.; Miyatake, K.; Hori, M.; Ota, K.; Ogumi, Z.; Miyata, S.; Nishikata, A.; Siroma, Z.; Uchimoto, Y.; Yasuda, K.; Kimijima, K. I.; Iwashita, N. *Chem. Rev.* **2007**, *107*, 3904.
- (4) Liu, Z. Y.; Zhang, J. L.; Yu, P. T.; Zhang, J. X.; Makharia, R.; More, K. L.; Stach, E. A. *J. Electrochem. Soc.* **2010**, *157*, B906.
- (5) Yu, P. T.; Gu, W.; Zhang, J.; Makharia, R.; Wagner, F. T.; Gasteiger, H. A. In *Polymer Electrolyte Fuel Cell Durability*; Büchi, F. N., Inaba, M., Schmidt, T. J., Eds.; Springer Science + Business Media LLC.: New York, 2009; p 29.
- (6) Smith, M. C.; Gilbert, J. A.; Mawdsley, J. R.; Seifert, S.; Myers, D. J. *J. Am. Chem. Soc.* **2008**, *130*, 8112.
- (7) Jang, S. E.; Kim, H. *J. Am. Chem. Soc.* **2010**, *132*, 14700.
- (8) Avasarala, B.; Moore, R.; Haldar, P. *Electrochim. Acta* **2010**, *55*, 4765.
- (9) Ball, S. C.; Hudson, S. L.; Thompsett, D.; Theobald, B. *J. Power Sources* **2007**, *171*, 18.
- (10) Hu, J. W.; Sui, P. C.; Kumar, S.; Djilali, N. *Electrochim. Acta* **2009**, *54*, 5583.
- (11) Liu, Z. Y.; Brady, B. K.; Carter, R. N.; Litteer, B.; Budinski, M.; Hyun, J. K.; Muller, D. A. *J. Electrochem. Soc.* **2008**, *155*, B979.
- (12) Maass, S.; Finsterwalder, F.; Frank, G.; Hartmann, R.; Merten, C. *J. Power Sources* **2008**, *176*, 444.
- (13) Ettingshausen, F.; Kleemann, J.; Michel, M.; Quintus, M.; Fuess, H.; Roth, C. *J. Power Sources* **2009**, *194*, 899.
- (14) Takeuchi, N.; Fuller, T. F. *J. Electrochem. Soc.* **2008**, *155*, B770.
- (15) Chang, C. L.; Chang, T. C.; Ho, W. Y.; Hwang, J. J.; Wang, D. Y. *Surf. Coat. Technol.* **2006**, *201*, 4442.
- (16) Li, M. F.; Tao, Q. A.; Liao, L. W.; Xu, J.; Cai, J.; Chen, Y. X. *Chin. J. Chem. Phys.* **2010**, *23*, 442.
- (17) Lim, K. H.; Oh, H. S.; Jang, S. E.; Ko, Y. J.; Kim, H. J.; Kim, H. *J. Power Sources* **2009**, *193*, 575.
- (18) Mayrhofer, K. J. J.; Meier, J. C.; Ashton, S. J.; Wiberg, G. K. H.; Kraus, F.; Hanzlik, M.; Arenz, M. *Electrochem. Commun.* **2008**, *10*, 1144.
- (19) Mayrhofer, K. J. J.; Ashton, S. J.; Meier, J. C.; Wiberg, G. K. H.; Hanzlik, M.; Arenz, M. *J. Power Sources* **2008**, *185*, 734.
- (20) Tang, H.; Qi, Z. G.; Ramani, M.; Elter, J. F. *J. Power Sources* **2006**, *158*, 1306.
- (21) Xu, F.; Wang, M. X.; Liu, Q.; Sun, H. F.; Simonson, S.; Ogbeifun, N.; Stach, E. A.; Xie, J. A. *J. Electrochem. Soc.* **2010**, *157*, B1138.
- (22) Young, A. P.; Stumper, J.; Gyenge, E. *J. Electrochem. Soc.* **2009**, *156*, B913.
- (23) Wilson, J. R.; Kobsiriphat, W.; Mendoza, R.; Chen, H. Y.; Hiller, J. M.; Miller, D. J.; Thornton, K.; Voorhees, P. W.; Adler, S. B.; Barnett, S. A. *Nat. Mater.* **2006**, *5*, 541.
- (24) Wilson, J. R.; Duong, A. T.; Gameiro, M.; Chen, H. Y.; Thornton, K.; Mumm, D. R.; Barnett, S. A. *Electrochem. Commun.* **2009**, *11*, 1052.
- (25) Wilson, J. R.; Gameiro, M.; Mischaikow, K.; Kalies, W.; Voorhees, P. W.; Barnett, S. A. *Microsc. Microanal.* **2009**, *15*, 71.
- (26) Wilson, J. R.; Scott Cronin, J.; Barnett, S. A.; Harret, S. J. *J. Power Sources* **2011**, *196*, 3443.
- (27) Ziegler, C.; Thiele, S.; Zengerle, R. *J. Power Sources* **2011**, *196*, 2094.
- (28) Schulenburg, H.; Roth, C. In *Polymer electrolyte membrane and direct methanol fuel cell technology (PEMFCs and DMFCs)*; Hartnig, C., Roth, C., Eds.; Woodhead Publishing Ltd.: Cambridge, U.K., 2011; Vol. 2.
- (29) Schulenburg, H.; Schwanitz, B.; Krbanjevic, J.; Linse, N.; Mokso, R.; Stampanoni, M.; Wokaun, A.; Scherer, G. G. *ECS Trans.* **2010**, *33*, 1471.
- (30) Zils, S.; Timpel, M.; Arlt, T.; Wolz, A.; Manke, I.; Roth, C. *Fuel Cells* **2010**, *10*, 966.
- (31) Ishitani, T.; Ohnishi, T.; Yaguchi, T. In *Nanofabrication: Fundamentals and Applications*; Tseng, A. A., Ed.; World Scientific Co. PTE. LTD.: Singapore, 2008; p 448.
- (32) Ender, M.; Joos, J.; Carraro, T.; Ivers-Tiffée, E. *Electrochem. Commun.* **2011**, *13*, 166.
- (33) Cody, G. D.; Davis, A. *Energy Fuel* **1991**, *5*, 776.
- (34) Hildebrand, T.; Rueggsegger, P. *J. Microsc. (Oxford, U.K.)* **1997**, *185*, 67.
- (35) Frank, J. *Electron Tomography: Methods for Three-Dimensional Visualization of Structures in the Cell*; Springer: Berlin, 2006.
- (36) Grothausmann, R.; Manke, I.; Zehl, G.; Dorbandt, I.; Bogdanoff, P.; Fiechter, S.; Hentschel, M. P.; Lange, A.; Kupsch, A.; Hilger, A.; Banhart, J. *MP Mater. Test.* **2010**, *52*, 706.
- (37) Friedrich, H.; de Jongh, P. E.; Verkleij, A. J.; de Jong, K. P. *Chem. Rev.* **2009**, *109*, 1613.
- (38) Koster, A. J.; Deruijter, W. J.; Vandenbos, A.; Vandermaast, K. D. *Ultramicroscopy* **1989**, *27*, 251.
- (39) Kremer, J. R.; Mastronarde, D. N.; McIntosh, J. R. *J. Struct. Biol.* **1996**, *116*, 71.
- (40) Reiser, C. A.; Bregoli, L.; Patterson, T. W.; Yi, J. S.; Yang, J. D. L.; Perry, M. L.; Jarvi, T. D. *Electrochem. Solid-State Lett.* **2005**, *8*, A273.
- (41) McCaffrey, J. P.; Phaneuf, M. W.; Madsen, L. D. *Ultramicroscopy* **2001**, *87*, 97.
- (42) Rubanov, S.; Munroe, P. R. *J. Microsc. (Oxford, U.K.)* **2004**, *214*, 213.
- (43) Ito, T.; Matsuwaki, U.; Otsuka, Y.; Katagiri, G.; Kato, M.; Matsubara, K.; Aoyama, Y.; Jinnai, H. In *Handbook of Fuel Cells—Fundamentals, Technology and Applications*; Advances in Electrocatalysis, Materials, Diagnostics and Durability; Vielstich, W., Yokokawa, H., Gasteiger, H. A., Eds.; John Wiley & Sons: New York, 2009; Vol. 6.
- (44) Grothausmann, R.; Manke, I. In preparation.
- (45) Linse, N.; Gubler, L.; Wokaun, A.; Scherer, G. G. In preparation.
- (46) Roen, L. M.; Paik, C. H.; Jarvic, T. D. *Electrochem. Solid-State Lett.* **2004**, *7*, A19.
- (47) Li, W.; Lane, A. M. *Electrochem. Commun.* **2009**, *11*, 1187.
- (48) Willsau, J.; Heitbaum, J. *J. Electroanal. Chem.* **1984**, *161*, 93.
- (49) Fiji Website. <http://pacific.mpi-cbg.de> (2011).